Experimental and theoretical evaluation of rotating orthogonal polarization imaging

Qun Zhu
Ian M. Stockford
John A. Crowe
Stephen P. Morgan
University of Nottingham
Electrical Systems and Optics Research Division
Faculty of Engineering
University Park
Nottingham NG7 2RD
United Kingdom
steve.morgan@nottingham.ac.uk

Abstract. Rotating orthogonal polarization imaging is a new technique that provides quantitative measurements of the polarization properties of scattering media, such as tissue, which are free from surface reflections. The technique is investigated using both experiments and Monte Carlo simulations of a polarizing target embedded within a scattering medium. The technique is sensitive to the polarization properties of the target up to a depth of 17 mean free paths. Preliminary images of bovine tendon, lamb tendon, chicken breast, and human skin are also demonstrated. [DOI: 10.1117/1.3130268]

Keywords: Polarization; orthogonal; surface reflection; scattering; tissue.

Paper 08383R received Oct. 27, 2008; revised manuscript received Feb. 22, 2009; accepted for publication Mar. 13, 2009; published online May 14, 2009. This paper is a revision of a paper presented at the SPIE conference on Optics in Tissue Engineering and Regenerative Medicine II, January 2008, San Jose, California. The paper presented there appears (unrefereed) in SPIE Proceedings Vol. 6858.

1 Introduction

Polarized light has many applications in biomedical optics. It has been demonstrated to be capable of providing coarse optical sectioning, which can be useful in characterizing superficial tissue.[1–4] In addition, many tissue types are known to have polarization properties that affect the polarization state of light such as linear dichroism in sickled red blood cells,[5] linear birefringence in collagen,[6] and chiral rotation in glucose.[7] Noninvasively characterizing the polarization properties of tissues has potential for *in vivo* clinical applications, such as monitoring the healing state of wounds and burns. In arthroscopic surgery, the alignment of collagen within tendons and ligaments can be measured through its polarization properties (birefringence and dichroism). In sickle cell anaemia, red blood cells polymerize and become linearly dichroic when they are deoxygenated.[5] Other potential applications include skin cancer diagnosis, plastic surgery, connective tissue disorders, endoscopy, and monitoring of tissue engineered structures in bioreactors.

Characterizing the polarization properties of tissues usually involves polarization difference imaging of the tissues (i.e., polarized light illumination and subtraction of the co- and cross-polarized detections). For clinical convenience, imaging in the backscattered direction is usually performed. However, in this case, the coimage is often dominated by surface reflections at the air-tissue interface, which obscures the polarization information from deeper tissue.[1,4,8] Therefore, accurate quantitative measurements of polarization difference signals are severely hampered by surface reflections.

It is well known that illuminating with linearly polarized light and detecting in the orthogonal (cross-)polarization state can be used to reduce the effects of surface reflections and improve image quality in tissue imaging.[9–11] This has been applied frequently in dermatoscopy[11] and in capillaroscopy[9] (imaging the microvasculature), and is often used in machine vision[12] and photography.[10] When imaging the microvasculature, this technique is known as orthogonal polarization spectral (OPS) imaging.[9] However, this does not permit quantification of the polarization properties of the underlying tissue because effective measurements can only be performed in the orthogonal polarization channel. Two alternative methods of reducing the effect of surface reflections are side-stream dark field illumination[13] and dark-field epi-illumination,[14] where source and detection are spatially displaced to remove the effects of surface reflections. In addition, Jacques et al.[1] proposed the use of matching fluid and a glass plate to overcome the surface reflection problem. In this case, the surface-reflected light is specularly reflected away from the detector by the glass plate; however, in many applications (e.g., endoscopy and assessment of wound healing), the use of matching fluid and a glass plate is not appropriate. Morgan and Stockford[4] proposed a subtraction of circular and linear polarization states in which the reversal of the helicity of surface-reflected circularly polarized light allows it to be differentiated from polarization maintaining light that enters the tissue. Boulbry et al.[8] have suggested an ellipsometric approach to measuring polarization difference signals, although this involves comparatively sophisticated instrumentation.

Recently, we have demonstrated[15] the basic principles of a new technique called rotating orthogonal polarization imaging (ROPI). This provides quantitative measurements of the polarization properties of scattering media, such as tissue, which are free from surface reflections. The technique involves illumination in a single polarization state and detection in the orthogonal polarization state. Synchronously rotating both the illumination and orthogonal detection states provides an im-

Address all correspondence to: Stephen Morgan, University of Nottingham, School of Electrical and Electronic Engineering, University Park-Nottingham, NG7 2RD United Kingdom.

1083-3668/2009/14(3)/034006/10/$25.00 © 2009 SPIE

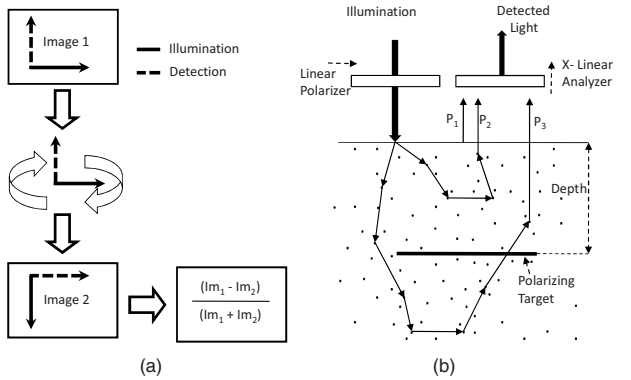

Fig. 1 (a) Formation of ROPI images and (b) typical photon trajectories in ROPI for a single illumination state. P_1 and P_2 are a surface reflection and weakly scattered component that are rejected as they maintain the original polarization state, and P3 is a path that has its polarization state modified by the target.

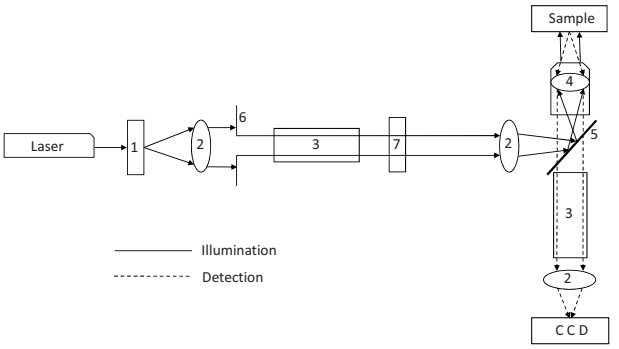

Fig. 2 ROPI experiment setup: (1) Ground glass rotating diffuser, (2) positive achromatic doublet lens, focal length=60 mm, (3) Glan–Thompson polarizer, (4) ×4 microscope infinite conjugate objective, NA=0.1,5) cubebeam splitter, (6) aperture, and (7) half-wave plate

age free from surface reflections that is sensitive to the polarization properties of the underlying scattering medium.

Sections 2–4 describe the technique, the experimental setup, and the Monte Carlo simulation model, respectively. Section 5 presents measurement results from phantom experiments and simulations together with preliminary images of tissue. Discussions and conclusions follow in Sections 6 and 7.

2 ROPI

The basic principle of applying ROPI for measuring the polarization properties of a target embedded within a scattering medium is shown in Fig. 1. Light illuminates the tissue in a linear polarization state, and detection is performed in the cross-polarization state [Fig. 1(a)]. Light that is reflected by the surface or is weakly scattered within superficial tissue maintains its original polarization state and is rejected by the cross-polar detection [paths P_1 and P_2 in Fig. 1(b)]. Light that has been multiply scattered within the tissue becomes randomly polarized and back-illuminates the target [path P_3, Fig. 1(b)]. Similar to OPS systems, this provides an image free from surface reflections. If the target possesses linear dichroism, then the randomly polarized field, which back-illuminates the target, has polarization information superimposed on it. The conventional way to analyze this polarization information superimposed by the target would be to perform co- and cross-polar detection but the copolar channel is dominated by surface reflections. For ROPI, both illumination and detection polarization states are rotated to maintain orthogonal detection [Fig. 1(a)]. A polarization difference image of these two cases provides a polarization-sensitive image of the medium that is free from surface reflections.

If it is assumed that the light that back-illuminates the target is randomly polarized, then it should be noted that the technique is only sensitive to linear dichroism and not birefringence. This is because purely birefringent tissue introduces a phase change into a randomly polarized field, which produces another randomly polarized field with no additional information. A Mueller matrix explanation of this effect, and the effect of linear dichroism on the randomly polarized field is presented in the Appendix.

3 Experimental Setup

The experimental setup is shown in Fig. 2. Polarized light from a HeNe laser (Power=20 mW, λ=632.8 nm) passes through a rotating ground glass diffuser, a collection lens, a Glan–Thompson polarizer, and a half-wave plate to control the polarization state of the illumination. Collimated light is focused via a cube beamsplitter to the back focal plane of a ×4, NA=0.1 infinite conjugate microscope objective, which provides nominally uniform illumination at the sample. An image of the sample is formed on the CCD camera (Hamamatsu ORCA ERII) via the objective, beamsplitter, a Glan–Thompson polarizer aligned in the orthogonal polarization state to the illumination, and a relay lens.

The tissue phantom comprises a cuvette (illuminated face dimensions 45×50 mm, depth 10 mm) filled with a suspension of polystyrene microspheres. The scattering medium has the properties described in Table 1, where g is the mean cosine of the scattering angle θ, an μ_a and μ_s are the absorption[16] and scattering coefficients of the medium at λ =632.8 nm. The mean free path (mfp) is the reciprocal of the

Table 1 Optical and physical properties of the scattering medium.

Parameter	Value
$g=\cos(\theta)$	0.93744
μ_s	20 mm^{-1}
μ_a	2.995×10^{-4} mm^{-1}
$mfp=1/\mu s$	0.05 mm
n_m	1.3316
n_p	1.5721
d	1.4 μm
λ	632.8 nm

scattering coefficient, n_m and n_p are the refractive indices of the medium and particles, respectively, and d is the particle diameter.

A 0.75-mm thick piece of sheet polarizer (8.5 $\times$0.65 mm) is embedded at different depths within the medium with its polarization axis horizontal. The extinction ratio of the target measured in a transmission experiment is 1×10^{-4}. In this case, as the polarization axis of the target is known (defined as 0 deg), only two pairs of orthogonal polarization states [(*i*) 0 deg illumination and 90 deg detection, (*ii*) 90 deg illumination and 0 deg detection] are needed to obtain the maximum contrast in the polarization difference images of the target. When the polarization axis of the target is unknown, it will be necessary to make at least three measurements to determine the alignment of the axis of the polarizing target, although it may be advantageous from a contrast and signal-to-noise perspective to synchronously rotate the illumination and detection polarization states over a range of angles. It should be noted that the polarization state of the light can be modified by scattering events between the target and the exit surface of the medium. This apparent change of dichroism with depth is discussed further in Section 6. An additional benefit of this technique in a coaxial system is that the orthogonal detection minimizes surface reflections from optical components within the system.

Ideally, the intensity distribution of light entering the medium should be uniform; however, in practice some nonuniformity is introduced after reflection from the beamsplitter. Therefore, before acquiring an image, the intensity is calibrated using a mirror in place of the scattering medium.

4 Monte Carlo Simulation

In this section, a modified Monte Carlo model developed to simulate ROPI measurements within a scattering medium is introduced. The basic principles of the model that we have developed have been described elsewhere.[17,18] The model simulates the propagation of individual photons through a scattering medium and tracks changes in a polarization state at each scattering event. Photons trajectories are terminated either when they exceed a predefined distance within the medium or they emerge from the medium and are detected. This allows us to build up the spatial and polarization properties of light emerging from a scattering medium. Absorption can be added postsimulation through application of the microscopic Lambert–Beer law. The mismatch in refractive index at the medium-air interface is taken into account by reflecting all those photons greater than or equal to the critical angle back into the medium.

In order to simulate the experiment described in Section 3, three modifications are necessary. The first allows full-field illumination to be obtained from a point source Monte Carlo simulation though indexing the position of photons. The second allows the insertion of a polarizing target into the scattering medium because, when a photon propagates through the target, the polarization properties are modified. The third allows representation of the appropriate imaging system.

4.1 *Full-Field Illumination*

It is computationally inefficient to run a separate Monte Carlo for each position on the input surface of the scattering medium. However, it is possible to run a single Monte Carlo simulation for a point illumination and then move this around the illumination plane provided. When there is a target present in the medium, it is important to record the possible interactions with the target by recording the positions that photons cross the target plane. Whether a photon has interacted with the target then depends on the relative position of the object and illumination.

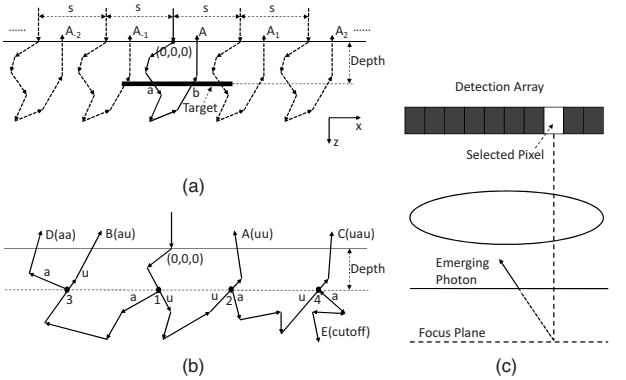

Fig. 3 Monte Carlo simulation: (a) index process for obtaining full-field illumination from a single point; (b) splitting process for photons that pass through the target plane, and (c) image formation.

Figure 3(a) shows a typical photon trajectory A obtained from a single Monte Carlo simulation. Through indexing, the illumination position can be displaced by a distance s to form photon paths A_{-n} to A_n. If the point that the photon crosses the target plane is recorded, then whether or not a photon has interacted with the target can be determined. We have found that setting $s=\mathrm{mfp}/4$ provides sufficient sampling at the illumination plane.

4.2 *Inserting a Polarizing Target within the Medium*

For the relatively straightforward case of a totally absorbing object, photons that have interacted with the target are absorbed and are not detected. However, here, the polarization state of the photon changes when it passes through a polarizing target. This provides a problem when using the indexing method for full-field illumination described previously because, depending on the relative position of illumination and object, some photons will have interacted with the target and some will not. A method of overcoming this problem is shown in Fig. 3(b). Each time a photon passes through the object plane, two new photon paths are generated; one for the case when the object does not interact with the target and one when it does. The Stokes vector of the photons that interact with the object are multiplied by the Mueller matrix for the polarizing target (as described in the Appendix), which produces a modified Stokes vector. The generation of new photon paths is repeated for multiple crossings of the object plane. In Fig. 3(b), the paths unaffected by the object are labeled u and the paths affected by the object are labeled a. For multiple crossings of the object plane, this eventually becomes computationally inefficient, but due to the small amount of attenuation within the background medium and the reduction in intensity when the polarization state of the photon is resolved in the axis of the target, these photons have a decreasing contribu-

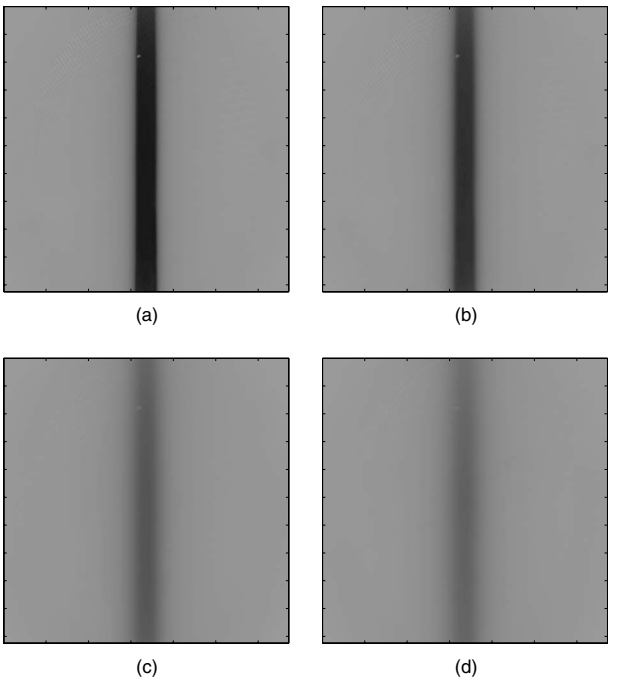

Fig. 4 Experimental ROPI images of a linear polarizer located at depths of (a) 2, (b) 5, (c) 10, and (d) 12 mfps within a scattering medium. The polarization axis of the target is horizontal (0 deg), the illumination is linearly polarized at 0 deg with 90 deg detection. Each image is 8×8 mm.

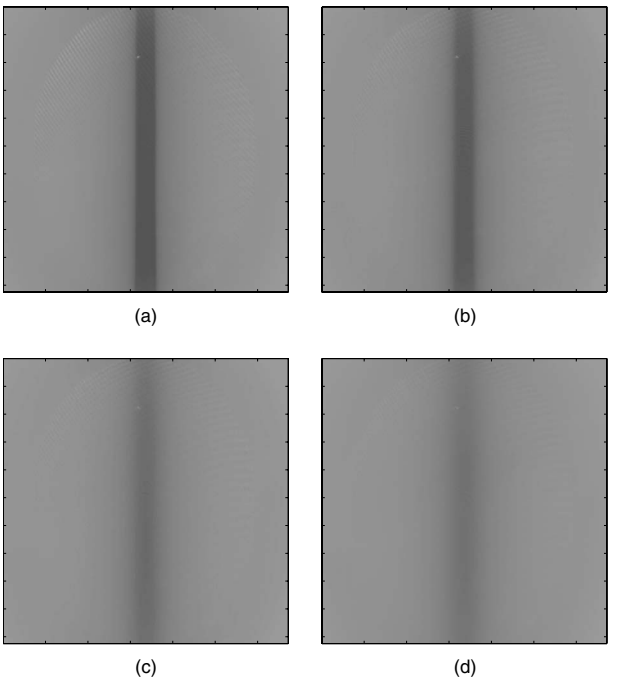

Fig. 5 Experimental ROPI images of a linear polarizer located at depths of (a) 2, (b) 5, (c) 10, and (d) 12 mfps within a scattering medium. The polarization axis of the target is horizontal (0 deg), the illumination is linearly polarized at 90 deg with 0 deg detection. Each image is 8×8 mm.

tion to the detected intensity. It has been found that ~20 crossings are required for the error to become insignificant.

The modeled results are compared to the experimental in Section 4.3. There are some differences between experiment and simulation. The main differences are that the target is assumed to be infinitely long in the vertical direction and infinitesimally thin in the depth direction. The refractive index of the polarizing target and the background is assumed to be the same and the polarizer is assumed to be ideal. For the simulations shown in Section 4.3, 512×512 points in x and y directions are used for full-field illumination, representing an area of 128 mfps $\times$ 128 mfps. The images are formed with five million photons launched into the medium with an overall detection area of 200 mfps $\times$ 200 mfps.

4.3 *Imaging System Representation*

In the image formation, the focal plane of the imaging system corresponds to the depth of the target and the imaging is performed by an infinite conjugate pair of lenses, such that an image of the focal plane is obtained at the detector. An image is formed by recording the angle of emergence of each photon at the surface and backpropagating to the focal plane of the optics. The x-y coordinates at this modified position are used to represent the position of the photon within the formed image as shown in Fig. 3(c).

5 Results

5.1 *Experiment*

The ROPI technique is demonstrated using images of a polarizer embedded within a scattering medium at depths of 2, 5,

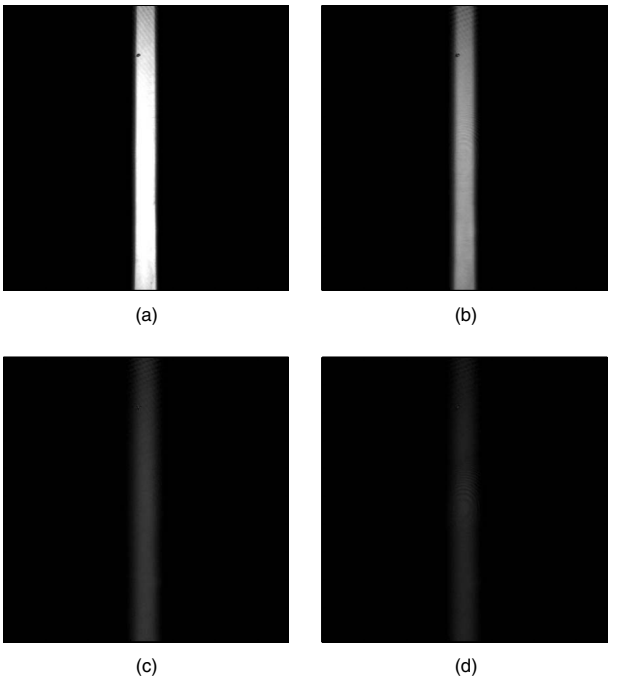

Fig. 6 Experimental ROPI images of the linear dichroism of a linear polarizer located at depths of (a) 2, (b) 5, (c) 10, and (d) 12 mfps within a scattering medium. The images are obtained by combining Figs 4 and 5. Each image is 8×8 mm.

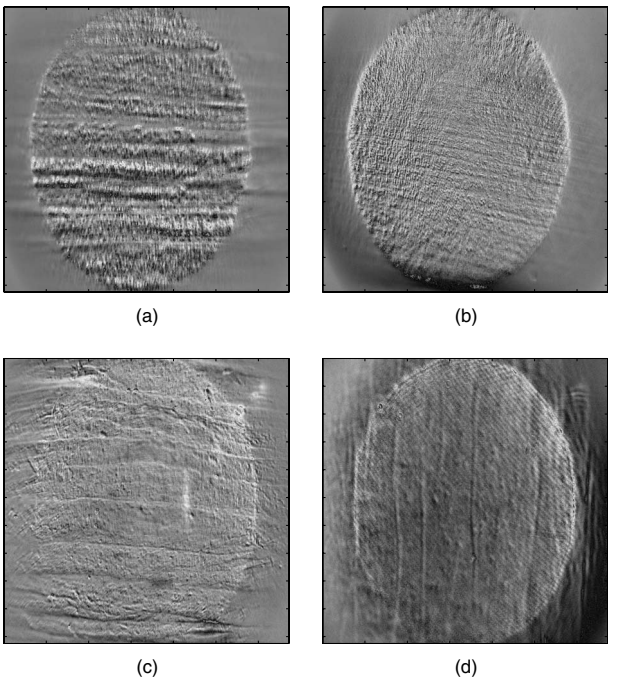

Fig. 7 ROPI normalized polarization difference of tissue images: (a) bovine tendon, (b) lamb tendon, (c) chicken breast, and (d) human left thumb inner skin. Each image is 8×8 mm.

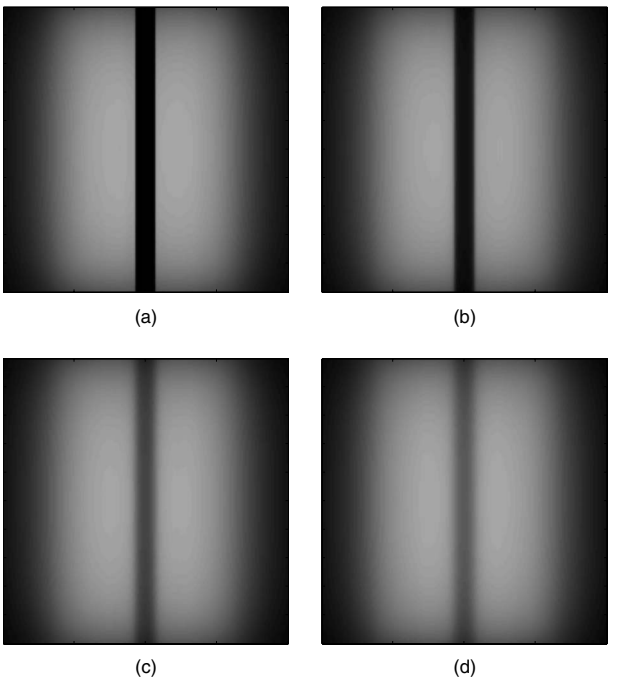

Fig. 8 Monte Carlo simulations of ROPI images of a linear polarizer located at depths of (a) 2, (b) 5, (c) 10, and (d) 12 mfps within a scattering medium. The polarization axis of the target is horizontal (0 deg), the illumination is linearly polarized at 0 deg with 90 deg detection. Each image is 200×200 mfps.

10, and 12 mfps (Figs. 4–6). As described in Section 3, because the target is aligned with its polarization axis horizontal (0 deg), imaging is only required at illumination/detection of 0 deg/90 deg and 90 deg/0 deg. Figure 4 shows the case with 0 deg polarized illumination (i.e., coaligned with the polarization axis of the target) and 90 deg polarized orthogonal detection, and Fig. 5 shows the case with 90 deg polarized illumination (i.e., cross-aligned with the polarization axis of the target) and 0 deg polarized orthogonal detection. In both cases, contrast clearly reduces with increasing depth due to the effects of scattering. The contrast is higher in the case of the coaligned illumination because the polarization state of detection in this case is orthogonal to the polarization axis of the target. The linear dichroism images shown in Fig. 6 are obtained by calculating the normalized polarization difference image [i.e., $(\text{image}_1-\text{image}_2)/(\text{image}_1+\text{image}_2)$ for the images shown in Figs. 4 and 5]. It can be seen that polarization-sensitive measurements that are free from surface reflections can still be obtained at the depth of 12 mfps within a scattering medium, but that the absolute measurement of dichroism is dependent on the depth of the polarizing target within the medium. The measured mean absolute values of the linear dichroism of the target are 0.66, 0.36, 0.12, and 0.08 for depths of 2, 5, 10, and 12 mfps, respectively. The depth limit of this technique for measuring a polarization difference of an embedded polarizer is ~17 mfps (images not shown).

Preliminary normalized polarization difference images obtained by ROPI of bovine tendon, lamb tendon, chicken breast, and human skin are shown in Fig. 7. The aperture in the illumination path is clearly visible in each of the images. To enhance the contrast of the images, a threshold is applied to remove outlying high- and low-intensity values before plotting the images using the *imagesc* function in Matlab. These results are free from surface reflections from both the tissue and the components within the system. Images obtained with the copolar system are dominated by surface reflections from the tissue surface and optical components and have been presented elsewhere[15] to demonstrate the improvement in performance achieved using ROPI. To provide an indication of the dynamic range of the system, it is useful to compare the polarization difference values for the highly organized bovine tendon tissue [Fig. 7(a)] and other tissue types to a suspension of polystyrene microspheres, which should not change the polarization properties of the medium. For the images shown in Figs. 7(a)–7(d), the mean absolute polarization difference values within the tissues are 0.07, 0.03, 0.027, and 0.013 respectively. For a microsphere solution (image not shown), the value is 0.003. Although these have not been validated using histology, they at least provide an indication that the technique is sensitive to the polarizing properties of the underlying tissue.

5.2 *Monte Carlo Simulations*

The Monte Carlo model has been used to simulate the experimental results shown in Figs. 4–6. A polarizing target that is 14 mfps wide, infinitely large in the vertical direction, and infinitely thin in the depth direction is embedded within a scattering medium. The target is placed at different depths within the scattering medium, and an image is formed by collecting all the photons that emerge at the surface within the detection area described in Section 4 and within the detection numerical aperture of the microscope objective used in the experiments.

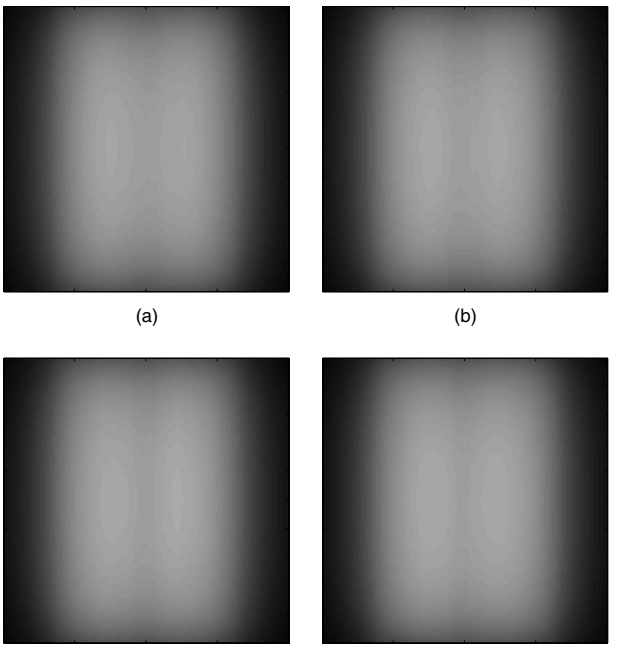

Fig. 9 Monte Carlo simulations of ROPI images of a linear polarizer located at depths of (a) 2, (b) 5, (c) 10, and (d) 12 mfps within a scattering medium. The polarization axis of the target is horizontal (0 deg), the illumination is linearly polarized at 90 deg with 0 deg detection. Each image is 200×200 mfps.

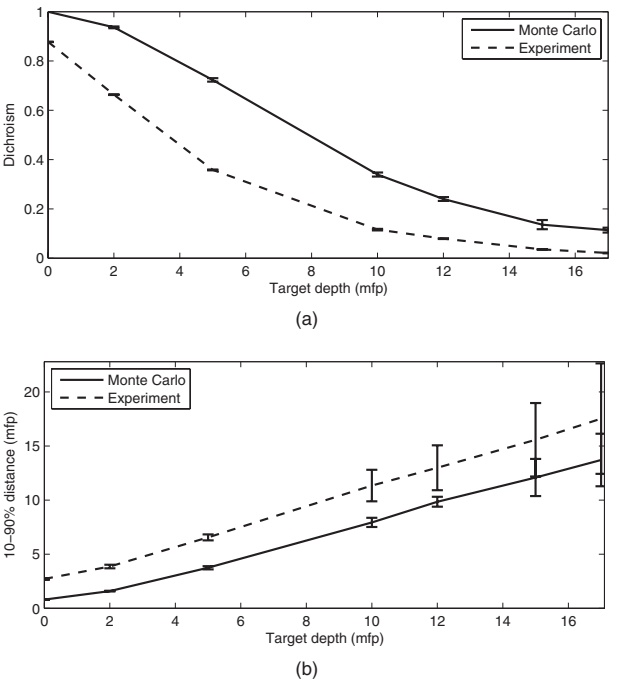

Fig. 11 Comparison of experimental and simulated polarization difference measurements of a polarizer embedded at different depths within a scattering medium (a) linear dichroism (b) resolution defined as the distance taken for the dichroism value to change from 10 to 90% of its maximum value.

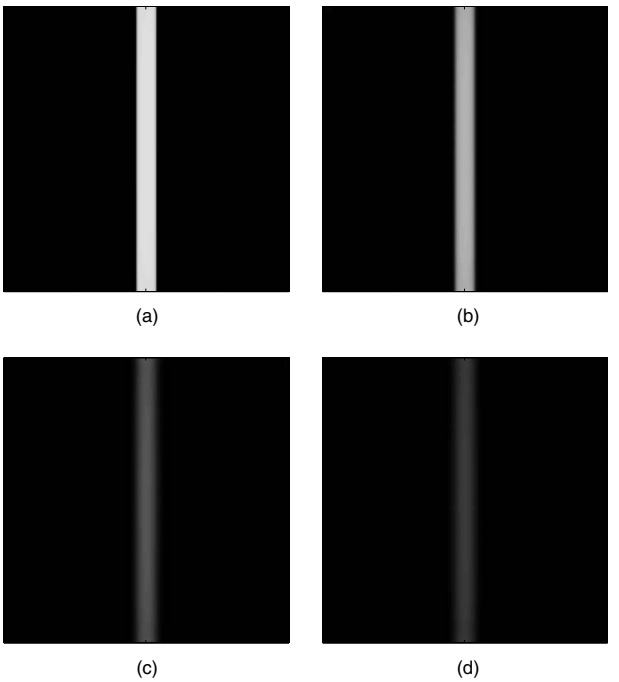

Fig. 10 Monte Carlo simulations of ROPI images of the linear dichroism of a linear polarizer located at depths of (a) 2, (b) 5, (c) 10, and (d) 12 mfps within a scattering medium. The images have been obtained by combining Figs. 8 and 9. Each image is 200×200 mfps.

Qualitatively, the results shown in Figs. 8–10 compare very well to those obtained experimentally (Figs. 4–6). All cases show degradation in image contrast and resolution with increasing depth due to scattering. Figure 8 shows the case where the polarization axis of the target is orthogonal to the polarization axis of the analyzer, resulting in a greater contrast compared to the case where the analyzer is aligned with the target (Fig. 9). The resulting simulated dichroism images are shown in Fig. 10.

A quantitative comparison of experiment and simulation over a range of depths is shown in Fig. 11. The dichroism values shown in Fig. 11(a) are obtained from the mean dichroism along a central vertical band of 200 pixels of the target in the dichroism images. The dichroism values obtained in the Monte Carlo simulation are higher than those obtained with the experiment across the entire depth range. The main source of error is due to reflections from the surface of the cuvette not being completely eliminated due to the finite rejection of the polarizer. It should be noted that, for this case, the surface reflections are directed back into the detection optics due to the flat and orthogonal surface. This represents the worst case of this contribution, which is anticipated to be lower for practical applications. However, due to careful alignment and calibration of the system these values of dichroism are considerably higher than those observed previously.[19] The 10–90% resolution distances are lower in the simulation than in the experiment, indicating a sharper edge response in the simulation. This is discussed in Section 6.

6 Discussion

It has been demonstrated that polarization-sensitive measurements that are free from surface reflections can still be obtained at a depth of 17 mfps within a scattering medium. However, the absolute measurement of dichroism is dependent on the depth of the polarizing target within the medium due to scattering effects between the target and the output surface of the cuvette. To enable accurate quantification of the dichroism of the target, the model can be used to provide a look up table for object depth and dichroism. Determining whether this is a well-conditioned problem is an important area of future research. It is likely that additional measurements such as multiple wavelengths or different illumination conditions will be required to provide a well-conditioned solution.

The Monte Carlo simulation provides results that qualitatively match those obtained in the experiment. There are several assumptions made in the model that cannot be accurately achieved in the experiment, such as ideal polarizers, precise depth location of the target, precise alignment of optical components, a refractive index match between the target and surrounding medium, an infinitely long and thin target, and uniform illumination.

Using the model, we have investigated the effects of nonideal polarizers, optical component alignment, numerical aperture, and depth location within the likely limits of experimental error. However, for the dichroism measurements [Fig. 11(a)], the dominant source of the discrepancy is caused by the surface of the cuvette introducing a contribution into the orthogonal detection channels. In principle, this should be completely removed by the analyzer but some reflections are still detected. This is particularly significant in the case when the target and analyzer are orthogonally aligned and the light intensity is low. Regarding the resolution against depth plot [Fig. 11(b)], the modeling results follow the same trend as the experiment. The main source of the difference between them is the finite thickness of the target, which results in the target occupying a range of depths.

To better simulate the phantom study, further refinements of the model could be performed, such as making the polarizers nonideal, the target of finite thickness or introducing surface reflections at the medium-target boundary. This is worthwhile for applications such as target detection in turbid water or imaging through fog, where the model provides an accurate representation of the real-world situation. For the tissue imaging problem, the focus should be on a more accurate model of the structure of the tissue.

It is important to consider how well the phantom experiment and its associated model represent real-world applications. The phantom study indicates that ROPI can provide sensitivity to polarization targets down to depths of 17 mfps. For typical tissue parameters,[20] this corresponds to a depth of 1.7 mm within tissue, which falls within the correct depth range for polarized light measurement of tissue.[20] Of course, the phantom represents the case of an isolated polarizing target embedded within a scattering medium. This is a reasonable approximation in capillaroscopy in the case of imaging isolated red blood cells in relatively homogeneous tissue for assessment of linear dichroism within cells for applications such as sickle cell anemia monitoring.[5,21] It is also reasonable for applications such as target location in turbid water or in fog[22] (albeit in both applications the target will have less polarization contrast than an isolated polarizer).

However, in other applications such as the monitoring of collagen alignment within tissue, the situation will be more complicated because the entire volume probed by the light will affect the polarization. It will be the subject future work to develop an inversion algorithm based on an appropriate model of the forward problem, such as that developed by Wang and Wang.[23] This algorithm will need validation through comparison to histology. Even without such an algorithm, the technique provides an indication of collagen alignment as demonstrated by the images shown in Fig. 7, which show polarization difference values for different types of tissue ranging from 0.07 for fibrous tendon down to 0.003 for a microsphere suspension. Through calibration with histology, such measurements could be useful for monitoring growth of tissue in bioreactors.

This paper has considered targets that exhibit linear dichroism, and it is important to consider the effect of birefringence on the measurement. If the light that "back-illuminates," the target is randomly polarized, then a birefringent target will not affect the output light from the medium. The Mueller matrix demonstration of this is shown in the Appendix. For birefringence to be detected, it is necessary for polarized light to reach the target plane, have its polarization state modified, and then to return to the detector plane with some preservation of the modified polarization state. Previous studies[24] (also validated by our Monte Carlo model described in this paper) have shown that linearly polarized light can probe depths of 34 mfps and that deeper propagation (102 mfps) can be obtained with circularly polarized light. It is also interesting to note that aligned structures, such as chicken breast may allow polarized light to propagate even further,[25] thereby allowing monitoring of birefringence at greater depths than could be obtained in homogeneous scattering media.

In our future research, we will modify the experiment to include liquid-crystal devices to allow easy rotation of the illumination and detection polarization states. This system will also reduce potential errors due to misalignment of the images before subtraction. This, of course, could also be overcome by software-based image alignment algorithms.[26]

7 Conclusions

Rotating orthogonal polarization imaging has been demonstrated by both phantom studies and Monte Carlo simulation. The technique involves illumination with polarized light and detection in the orthogonal polarization state. Rotating both the illumination and detection polarization states to maintain orthogonal detection allows polarization-sensitive measurements of the underlying tissue to be obtained that are free from surface reflections. These reflections can be from the air-tissue interface and also from optical components within a coaxial imaging system. The simulation is substantially different from a conventional polarized light Monte Carlo because it performs full-field illumination and includes the introduction of a target that can modify the polarization state of the light.

Polarization-sensitive measurements of a polarizing target embedded at a depth of 17 mfps within a scattering medium

can be made. The Monte Carlo model demonstrates the same trends as the experiment, but several ideal assumptions have been made in the model, which results in a difference in measurements of linear dichroism and resolution of the target at different depths.

Preliminary tissue results have shown the potential for making polarization sensitive measurements of tissues such as tendon and skin. Further work is necessary to develop the inversion algorithms necessary to ensure that the measurements are quantitatively meaningful.

Appendix

Some simple Mueller calculus can be used to demonstrate ideal ROPI measurements of linear dichroism (strictly speaking at a single wavelength, diattenuation) and birefringence.

Dichroism Measurement

Consider the imaging arm of the ROPI system shown in Fig. 2. The following assumptions are made to demonstrate the main principles of the technique;

1. Surface reflections are eliminated as the detection is orthogonal to the illumination.

2. The majority of light undergoes many scattering events, and thus, the light that back-illuminates the target is randomly polarized.

3. The polarization state imposed on the light by the target is maintained until detection.

Diattenuation measurements are taken in two orthogonal detection polarization states, and the normalized difference is calculated. It should be noted that these assumptions (also made in capillaroscopy[9]) greatly simplify the derivation. They are valid in many cases, but when the target is close to the surface of the scattering medium, then it is possible to have polarization-maintaining light illumination of the target.

The randomly polarized light, which backilluminates the target, is represented by the Stokes' vector $\vec{S}_i$, where

$$\vec{S}_i = \begin{bmatrix} 1 \\ 0 \\ 0 \\ 0 \end{bmatrix}. \tag{1}$$

The Mueller matrix of a general diattenuator, $\vec{M}_D$ can be shown to be[27]

$$\vec{M}_{\mathrm{D}} = \frac{T_1 + T_2}{2} \times \begin{bmatrix} 1 & \frac{T_1 - T_2}{T_1 + T_2}\cos(2\varphi) & \frac{T_1 - T_2}{T_1 + T_2}\sin(2\varphi) & 0 \\ \frac{T_1 - T_2}{T_1 + T_2}\cos(2\varphi) & \frac{2\sqrt{T_1 T_2}}{T_1 + T_2} + \left(1 - \frac{2\sqrt{T_1 T_2}}{T_1 + T_2}\right)\cos^2(2\varphi) & \left(1 - \frac{2\sqrt{T_1 T_2}}{T_1 + T_2}\right)\cos(2\varphi)\sin(2\varphi) & 0 \\ \frac{T_1 - T_2}{T_1 + T_2}\sin(2\varphi) & \left(1 - \frac{2\sqrt{T_1 T_2}}{T_1 + T_2}\right)\cos(2\varphi)\sin(2\varphi) & \frac{2\sqrt{T_1 T_2}}{T_1 + T_2} + \left(1 - \frac{2\sqrt{T_1 T_2}}{T_1 + T_2}\right)\sin^2(2\varphi) & 0 \\ 0 & 0 & 0 & \frac{2\sqrt{T_1 T_2}}{T_1 + T_2} \end{bmatrix}, \tag{2}$$

where T_1 and T_2 are the transmittances of the diattenuator along the major and minor axes, respectively, and φ is the azimuthal angle of the diattenuator. The Stokes' vector representing light emerging from the sample, $\vec{S}_S$, (assuming no loss of polarization information due to scattering between the diattenuator and the surface) is given as:

$$\vec{S}_{\mathrm{S}} = \vec{M}_{\mathrm{D}} \times \vec{S}_i = \begin{bmatrix} \frac{T_1 + T_2}{2} \\ \frac{T_1 - T_2}{2}\cos(2\varphi) \\ \frac{T_1 - T_2}{2}\sin(2\varphi) \\ 0 \end{bmatrix}. \tag{3}$$

The Mueller matrix of an arbitrarily orientated linear polarizer, $\vec{M}_P$, through which detection is performed, is defined as[28]

$$\vec{M}_{\mathrm{P}}(\theta) = \frac{1}{2}\begin{bmatrix} 1 & \cos(2\theta) & \sin(2\theta) & 0 \\ \cos(2\theta) & \cos^2(2\theta) & \cos(2\theta)\sin(2\theta) & 0 \\ \sin(2\theta) & \cos(2\theta)\sin(2\theta) & \sin^2(2\theta) & 0 \\ 0 & 0 & 0 & 0 \end{bmatrix}, \tag{4}$$

where θ is the azimuthal angle of the analyzing linear polarizer. Therefore, the intensities detected in orthogonal linear polarization states (analyzers at θ_1 and $\theta_1 + \pi/2$) are given by

$$I(\theta_1) = \frac{T_1 + T_2}{4} + \frac{T_1 - T_2}{4}\cos(2\theta_1)\cos(2\varphi) + \frac{T_1 - T_2}{4}\sin(2\theta_1)\sin(2\varphi)$$

$$I\left(\theta_1+\frac{\pi}{2}\right)=\frac{T_1+T_2}{4}+\frac{T_1-T_2}{4}\cos(2\theta_1+\pi)\cos(2\varphi)+\frac{T_1-T_2}{4}\sin(2\theta_1+\pi)\sin(2\varphi)=\frac{T_1+T_2}{4}-\frac{T_1-T_2}{4}\cos(2\theta_1)\cos(2\varphi)-\frac{T_1-T_2}{4}\sin(2\theta_1)\sin(2\varphi). \quad (5)$$

The diattenuation D_L (linear dichroism) relative to the angle θ_1 is

$$D_L=\frac{I(\theta_1)-I(\theta_1+\pi/2)}{I(\theta_1)+I(\theta_1+\pi/2)}. \quad (6)$$

Combining (5) and (6)

$$D_L=\frac{T_1-T_2}{T_1+T_2}\{\cos(2\theta_1)\cos(2\varphi)+\sin(2\theta_1)\sin(2\varphi)\}=\frac{T_1-T_2}{T_1+T_2}\cos\{2(\theta_1-\varphi)\}=\frac{T_1-T_2}{T_1+T_2}\cos(\Delta\gamma), \quad (7)$$

where $\Delta\gamma=2(\theta_1-\phi)$

Clearly, from Eq. (7), the diattenuation (linear dichroism) varies cosinusoidally from a minimum of 0 when $\Delta\gamma=90$ deg to a maximum of $(T_1-T_2)/(T_1+T_2)$ when $\Delta\gamma=90$ deg. The linear dichroism depends on the difference between the azimuthal angles of the diattenuator and analyzing polarizer and the transmittances of the diattenuator along the major and minor axes.

For the case investigated in this paper, $\varphi=0$ and $\theta_1=0$,

$$D_L=\frac{T_1-T_2}{T_1+T_2}. \quad (8)$$

This demonstrates that measurements of diattenuation can be made with randomly polarized backillumination.

Birefringence Measurement

Measurement of birefringence cannot be performed when the assumption is made that the back-illuminating light is randomly polarized. Consider the Mueller matrix for a birefringent target,[28]

$$\vec{M}_B=\begin{bmatrix}1 & 0 & 0 & 0\\ 0 & \cos^2(2\zeta)+\sin^2(2\zeta)\cos\delta & (1-\cos\delta)\sin(2\zeta)\cos(2\zeta) & -\sin(2\zeta)\sin\delta\\ 0 & (1-\cos\delta)\sin(2\zeta)\cos(2\zeta) & \sin^2(2\zeta)+\cos^2(2\zeta)\cos\delta & \cos(2\zeta)\sin\delta\\ 0 & \sin(2\zeta)\sin\delta & -\cos(2\zeta)\sin\delta & \cos\delta\end{bmatrix}, \quad (9)$$

where ζ is the azimuthal orientation of the fast axis of the component and δ is the phase delay in wavelengths.

Backillumination of the birefringent target with randomly polarized light results in the following Stokes' vector representing light emerging from the sample:

$$\vec{S}_S=\vec{M}_B\times\vec{S}_i=\vec{M}_B\times\begin{bmatrix}1\\0\\0\\0\end{bmatrix}=\begin{bmatrix}1\\0\\0\\0\end{bmatrix}, \quad (10)$$

which represents randomly polarized light. Therefore, it is clear that randomly polarized backillumination cannot be used to extract information regarding sample birefringence. This is, of course, based on the assumption that the light that reaches the target is randomly polarized. If the polarizing target is positioned at a depth where polarized light is able to interact with the target, then polarization-sensitive measurements of birefringence can also be made.

Acknowledgments

The authors acknowledge support from the Engineering and Physical Sciences Research Council (Grant No. EP/C534247/1). Q. Zhu was funded by a studentship from the international office at the University of Nottingham. We also acknowledge the assistance of Dr. N B E. Sawyer in setting up the initial experiment.

References

1. S. L. Jacques, J. R. Roman, and K. Lee, "Imaging superficial tissues with polarized light," *Lasers Surg. Med.* **26**, 119–129 (2000).
2. S. G. Demos and R. R. Alfano, "Optical polarization imaging," *Appl. Opt.* **36**, 150–155 (1997).
3. V. Backman, R. Gurjar, K. Badizadegan, L. Itzkan, R. R. Dasari, L. T. Perelman, and M. S. Feld, "Polarized light scattering spectroscopy for quantitative measurement of epithelial cellular structures *in situ*," *IEEE J. Sel. Top. Quantum Electron.* **5**, 1019–1026 (1999).
4. S. P. Morgan and I. M. Stockford, "Surface reflection elimination in polarization imaging of superficial tissue," *Opt. Lett.* **28**, 114–116 (2003).
5. D. A. Beach, C. Bustamante, K. S. Wells, and K. M. Foucar, "Differential polarization imaging. 3. Theory confirmation–patterns of polymerization of haemoglobin-S in red blood sickle cells," *Biophys. J.* **53**, 449–456 (1988).
6. M. Morgan, O. Kostyuk, R. A. Brown, and V. Mudera, "*In situ* moni-

toring of tendon structural changes by elastic scattering spectroscopy: correlation with changes in collagen fibril diameter and crimp," *Tissue Eng.* **12**, 1821–1831 (2006).
7. R. J. McNichols and G. L. Cote, "Optical glucose sensing in biological fluids: an overview," *J. Biomed. Opt.* **5**, 5–16 (2000).
8. B. Boulbry, T. A. Germer, and J. C. Ramella-Roman, "A novel hemispherical spectro-polarimetric scattering instrument for skin lesion imaging," *Proc. SPIE* **6078**, 128–134 (2006).
9. W. Groner, J. W. Winkelman, A. G. Harris, C. Ince, G. J. Bouma, K. Messmer, and R. G. Nadeau, "Orthogonal polarization spectral imaging: a new method for study of the microcirculation," *Nat. Med.* **5**, 1209–1212 (1999).
10. R. R. Anderson, "Polarized-light examination and photography of the skin," *Arch. Dermatol.* **127**, 1000–1005 (1991).
11. A. A. C. Chuh, "The use of digital epiluminescence dermatoscopy to identify peripheral scaling in pityriasis rosea," *Comput. Med. Imaging Graph.* **26**, 129–134 (2002).
12. S. S. Lin, K. M. Yemelyanov, E. N. Pugh, Jr., and N. Engheta, "Separation and contrast enhancement of overlapping cast shadow components using polarization," *Opt. Express* **14**(16), 7099–7108 (2006).
13. C. Ince, "Sidestream dark field imaging: an improved technique to observe sublingual microcirculation," *Crit. Care* **9**(suppl 4), S13–S19 (2005).
14. J. J. Monari, "Human capillaroscopy by light emitting diode epi-illumination," *Microvasc. Res.* **59**, 172–175 (1999).
15. S. P. Morgan, Q. Zhu, I. M. Stockford, and J. A. Crowe, "Rotating orthogonal polarization imaging," *Opt. Lett.* **33**(13), 1503–1505 (2008).
16. R. M. Pope and E. S. Fry, "Absorption spectrum (380–700 nm) of pure water. II. Integrating cavity measurements," *Appl. Opt.* **36**, 8710–8723, (1997).
17. I. M. Stockford, S. P. Morgan, P. C. Y. Chang, and J. G. Walker, "Analysis of the spatial distribution of polarized light backscattered from layered media," *J. Biomed. Opt.* **7**, 313–320 (2002).
18. P. C. Y. Chang, J. G. Walker, K. I. Hopcraft, B. Ablitt, and E. Jakeman, "Polarization discrimination for active imaging in scattering media," *Opt. Commun.* **159**, 1–6 (1999).
19. S. P. Morgan, Q. Zhu, I. M. Stockford, and J. A. Crowe, "Rotating orthogonal polarization imaging for tissue imaging," *Proc. SPIE* **6858**, 68580A (2008).
20. V. V. Tuchin, *Tissue Optics*, SPIE Bellingham, WA (2007).
21. S. P. Morgan, I. M. Stockford, J. A. Crowe, and B. R. Hayes-Gill, "Optical imaging and spectroscopy of superficial tissue," *J. Innovat. Opt. Health Sci.* **1**, 85–93 (2008).
22. G. D. Lewis, D. L. Jordan, and P. J. Roberts, "Backscattering target detection in a turbid medium by polarization discrimination," *Appl. Opt.* **38**, 3937–3944 (1999).
23. X. D. Wang and L. H. V. Wang, "Propagation of polarized light in birefringent turbid media: a Monte Carlo study," *J. Biomed. Opt.* **7**, 279–290 (2002).
24. S. P. Morgan and M. E. Ridgway, "Polarization properties of light backscattered from a two layer scattering medium," *Opt. Express* **7**(12), 395–402 (2000).
25. C. W. Sun, C. Y. Wang, C. C. Yang, Y. W. Kiang, C. W. Lu, I. J. Hsu, and C. W. Lin, "Polarization-dependent characteristics and polarization gating in time-resolved optical imaging of skeletal muscle tissues," *IEEE J. Sel. Top. Quantum Electron.* **7**(6), 924–930 (2001).
26. N. B. E. Sawyer, S. P. Morgan, M. G. Somekh, C. W. See, X. F. Cao, B. Y. Shekunov, and E. Astrakharchik, "Wide field amplitude and phase confocal microscope with parallel phase stepping," *J. Opt. Soc. Am. A* **72**(10), 3793–3801 (2001).
27. S. Y. Lu and R. A. Chipman, "Interpretation of Mueller matrices based on polar decomposition," *J. Opt. Soc. Am. A* **13**, 1106–1113 (1996).
28. W. S. Bickel and W. M. Bailey, "Stokes vector, Mueller matrices, and polarized scattered light," *Am. J. Phys.* **53**, 468–478 (1985).